

## ARTICLE

## OPEN

## Flash sintering incubation kinetics

K.S.N. Vikrant<sup>1</sup>, Han Wang<sup>1</sup>, Aniruddha Jana<sup>1</sup> , Haiyan Wang<sup>1,2</sup> and R. Edwin García<sup>1</sup>  

The microstructural mechanisms leading to onset of the flash sintering are demonstrated experimentally and theoretically for Yttria Stabilized Zirconia, YSZ. Three regimes leading to flash event are identified: (1) Radiation-dominated regime, where the oven controls the heating of the sintered sample, and a small subset of particle-particle contacts and surfaces of the green body define percolative paths for the charge to flow along and across the interfaces; (2) Transition regime, where charge transport is suppressed across particle contact misorientations and deflects to surficial and small angle particle contact misorientations. As a result, internal Joule heating takes over externally-driven radiation heating. Finally, (3) Percolative regime, where the concentration of oxygen vacancies drastically increases at particle contacts, surfaces, and triple junctions, and enables charge to flow through multiple paths, generating large amounts of Joule heating, resulting in the onset of a flash event. The validated theory sets the stage to rationalize the microstructural evolution and charge transport on a ceramic green body during flash sintering.

*npj Computational Materials* (2020)6:98; <https://doi.org/10.1038/s41524-020-00359-7>

## INTRODUCTION

The state-of-the-art of energy storage, biomedical, electronic, and high-temperature materials and devices demand a broad palette of ceramic materials with high-performance properties. Typically, these ceramic materials are manufactured using powder compacts fired at high temperatures to enhance mass transport and densification. This classic technique called *sintering*<sup>1</sup>, consumes large amounts of thermal energy, requires from hours to days of processing, and contributes a great deal to CO<sub>2</sub> emissions, increasing its manufacturing cost and making it detrimental to the environment<sup>2,3</sup>.

Modifications to this basic approach include the application of external mechanical pressure<sup>4</sup>, electric<sup>5</sup>, and magnetic fields<sup>6</sup> to decrease manufacturing cost, applied energy, and processing time. These new techniques enabled an unprecedented degree of control of grain size, porosity, and crystallographic texture. Specifically, flash sintering has emerged as a very promising processing technique<sup>5,7–11</sup>, for the fabrication of electronic<sup>12–14</sup>, semiconducting<sup>15–17</sup>, and composite solids<sup>18,19</sup>. Flash sintering was pioneered by Cologna, Rashkova, and Raj, and provides remarkably rapid densification, with processing times in the range of minutes to hours, at furnace temperatures significantly lower than those used by traditional sintering techniques<sup>5</sup>. 3YSZ was the first ceramic material processed using flash sintering<sup>5</sup>, see experimental results shown in Fig. 1. At a heating rate of 10 K/min, for a constant applied electric field of 60 V/cm, the onset furnace temperature for flash is measured as 1310 K. The increase in applied electric field from 60 to 120 V/cm reduces the onset temperature for flash to 1123 K<sup>5</sup>.

Flash sintered specimens are rapidly densified with a sudden increase in electrical conductivity, and is followed by a bright light emission event which is referred to as the flash event<sup>20</sup>. Also, a nonlinear increase in power density is experimentally reported in the 10 to 50 mW/mm<sup>3</sup> range for a wide variety of ceramics, for different temperatures and electric fields<sup>21</sup>. The range of observed power density is attributed to Joule heating, and correlates to the onset of flash<sup>21,22</sup>. As the sample builds up to the flash event, the total conductivity follows an Arrhenius-type behavior as a function

of the sample temperature. The onset condition for flash was first predicted using a coarse-grain thermal runaway model developed by Zhang, Jung, and Luo for ZnO<sup>23</sup>, Todd et al. for YSZ<sup>24</sup>, and also Dong and Chen for a portfolio materials<sup>25</sup>. Recent rapid thermal annealing experiments on ZnO<sup>26</sup>, and 3YSZ<sup>27</sup>, without an electric field achieved rapid densification rates analogous to flash sintered samples indicating that the heating rate of the sample is an important controlling factor for fast densification and grain growth rates.

To explain the underlying mechanisms that lead to the flash event, including thermal annealing approaches<sup>28</sup>, a wide range of mechanisms have been brought forward. Raj proposed the possibility of field-induced Frenkel pairs formation at particle contacts to facilitate the mass transport for flash sintering<sup>29</sup>. Naik et al. proposed the nucleation of Frenkel pairs at grain boundaries, but required an unphysically large dielectric constant contrast between grains and grain boundaries in order to contribute an inhomogeneous volumetric dipolar free energy that would drive the sintering process, while the grain boundaries experience large Joule heating<sup>30</sup>. Most recently, Jongmanns et al. suggested through molecular dynamics simulations on aluminum the possibility of large concentrations of Frenkel pairs for sample temperatures above the Debye temperature<sup>31</sup>. However, Schie et al.<sup>32</sup> reported that a substantially large field of 10 G/V/m is required to generate Frenkel pairs in ionic ceramics, using HfO<sub>2</sub> as a model material.

In contrast, Narayan proposed that electric fields alter the atomic mobility and enthalpy of migration of the diffusion process. Also, he proposed that the electric field would generate anionic vacancies as a result of the partial reduction of the material, which are preferentially segregated at grain boundaries and dislocation loops<sup>33</sup>. The excess vacancies are proposed to lead to localized Joule heating at grain boundaries, including the possibility of premelting, potentially leading to a flash event<sup>34</sup>.

Another mechanism that has been proposed to rationalize the onset of the flash event is based on the hypothetical development of significant temperature gradients where overheating/premelting of particle contacts define the abrupt increase in the electrical

<sup>1</sup>School of Materials Engineering, Purdue University, West Lafayette, IN 47907, USA. <sup>2</sup>School of Electrical and Computer Engineering, Purdue University, West Lafayette, IN 47907, USA.  email: redwing@purdue.edu

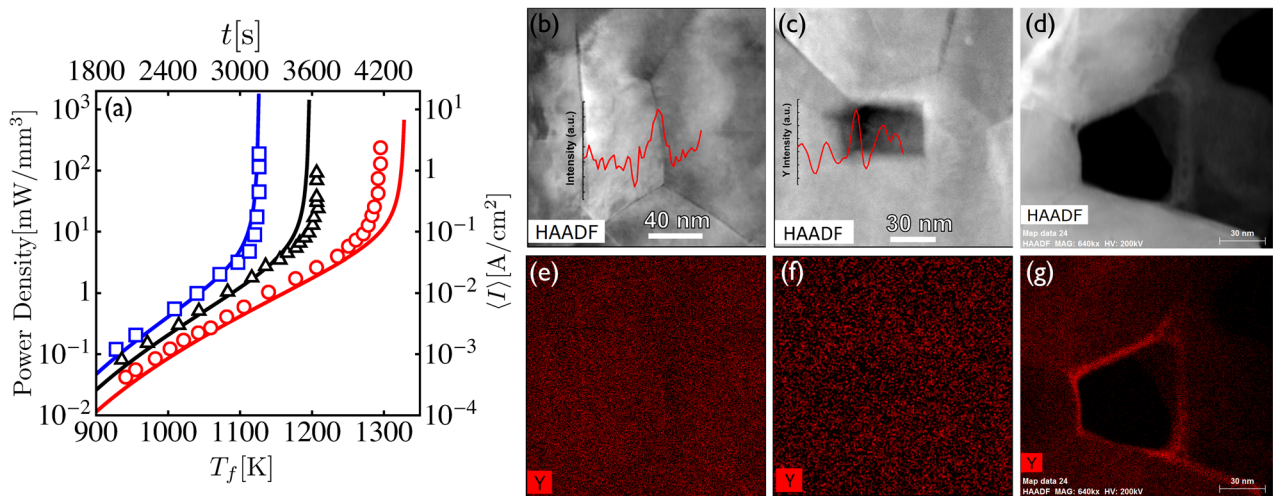


**Fig. 1 Macroscopic and microstructural features of flash sintered 3YSZ specimens.** Inset (a) experimental and predicted macroscopic power density and average current density, as a function of furnace temperature and time, for 3YSZ samples, subjected to a constant heating rate of 10 K/min, for three applied electric fields: 60 V/cm (red), 90 V/cm (black), and 120 V/cm (blue). Experimental corresponds to results reported by Cologna and coworkers (red circle, black triangle, blue square)<sup>5</sup>. HAADF-STEM micrographs for two flash sintered 3YSZ specimens of a grain boundary are shown in insets (b) and (d). A pore is shown in insets (c) and (d), for an applied electric field of 60 V/cm. The corresponding EDS mapping of interfacial and surficial  $[Y_{Zr}]$  distribution is shown in insets (e), (f), and (g).

conductivity. Here, particles and particle contacts soften and transform into liquid, potentially leading to a flash event<sup>35</sup>. However, because of the high thermal diffusivity of 3YSZ, heat transfers rapidly from local Joule heating hot spots, large thermal gradients for time-scales greater than  $\sim 1 \mu\text{s}$  cannot be physically justified<sup>24,36</sup>.

Experimentally, the detailed microstructural analysis of flash sintered samples of 3YSZ by M'Peko et al. indicates that there is a sudden increase of the concentration of oxygen vacancies near interfaces<sup>37</sup>. Additional Transmission Electron Microscopy studies on YSZ bicrystals by Yoshida et al. suggested that the increase in crystallographic misorientation facilitates yttrium segregation as a result of local disorder imposed by the interfacial energy<sup>38,39</sup>. Further, atomistic studies by Lee et al. highlight the segregation of oxygen vacancies and yttrium defects at interfaces followed by the development of depletion regions of defects in the immediate neighborhood of grain boundaries<sup>40,41</sup>.

Chen and Khachaturyan pioneered diffuse interface models to study the electrostatic and polarization effects in ionic solids<sup>42</sup>. Bishop and coworkers developed a thermodynamically consistent phase-field model for spinodal decomposition of charged domains in ionic ceramics<sup>43</sup>, and García et al. developed a generalized variational formulation which naturally includes Maxwell's Equations to describe the thermodynamics and kinetics of electrically active systems<sup>44</sup>. Separately, Guyer and coworkers proposed a phase-field theory to describe the local equilibrium of a double layer associated to an electrochemical interface<sup>45</sup>. Recently, Vikrant et al. introduced a variational formulation, which includes electrochemical and chemomechanical effects to describe the equilibrium space charge layers at a grain boundary and their associated transport properties<sup>46</sup>. Most recently, Vikrant and García applied this thermodynamic framework to understand the effect of misorientation and chemical dopant on the interfacial structural and electrochemical phase transitions and their overall impact on ionic transport properties<sup>47</sup>.

In spite of the rapid progress to harness the potential of flash sintering, a fundamental understanding of the mechanisms leading to the flash event remain unavailable. Further, the microstructural mechanisms controlling the incubation time and the critical power density necessary to flash are not known. In this paper, the very first thermodynamically consistent theory to

explain the mechanisms that lead to the flash event is presented by considering  $N$  chemical species,  $\{[V_j^z]\} = \{[V_1^z], \dots, [V_N^z]\}$ , of an ionic ceramic green body for three distinct microstructural regions,  $\{\eta_i\} = \{\eta_x, \eta_d, \eta_v\}$ . Here, each single crystal particle in a two-dimensional polycrystalline ionic ceramic green body is described using a crystallographic orientation order parameter,  $\theta$ . This description sets the stage to rationalize the concurrent microstructural evolution and charge transport on a ceramic green body during electric-field assisted sintering. For Yttria Stabilized Zirconia and following recent work on charged interfaces<sup>46,47</sup>, the sum of all the contributions from chemical, electrical, and interfacial energy to the total free energy functional is given by

$$\begin{aligned} F\{\eta_i\}, \{[V_j^z]\}, \theta, \rho, \phi; T &= \int_{\Omega} [f(\eta_x, \eta_d, \eta_v, [V_1^z], \dots, [V_N^z], T) \\ &\quad + \frac{a_x^2}{2} (\nabla \eta_x)^2 + \frac{a_d^2}{2} (\nabla \eta_d)^2 + \frac{a_v^2}{2} (\nabla \eta_v)^2 \\ &\quad + g(\eta_x)(s_1 |\nabla \theta| + \frac{s_2}{2} |\nabla \theta|^2) + \rho \phi - \frac{\epsilon}{2} (\nabla \phi)^2] d\Omega \end{aligned} \quad (1)$$

where  $f$  is the Helmholtz free energy per unit volume,  $a_x$  is the gradient energy coefficient of order-disorder interface,  $a_d$  is the gradient energy coefficient of disorder-porous interface,  $a_v$  is the gradient energy coefficient of porous-order interface,  $\rho$  is the electrostatic charge per unit volume,  $\phi$  is local electrostatic potential,  $g(\eta_x) = \eta_x^2$  is a coupling function, and  $s_1$  and  $s_2$  are structural coupling parameters, as presented by Kobayashi et al.<sup>48</sup>.

Locally, for small deviations away from equilibrium, the variational derivatives associated to Eq. (1) constitute the structural and electrochemical driving forces for microstructural evolution<sup>44,49</sup>. The resultant kinetic equations are

$$\begin{aligned} \frac{\partial \theta}{\partial t} &= M_\theta \left[ g(\eta_x)(s_1 \nabla \cdot \left[ \frac{\nabla \theta}{|\nabla \theta|} \right] + s_2 \nabla^2 \theta) \right] \\ \frac{\partial \eta_x}{\partial t} &= -M_{\eta_x} \left[ \frac{\partial f}{\partial \eta_x} - a_x^2 \nabla^2 \eta_x - \frac{a_d^2}{2} \nabla^2 \eta_v + \frac{\partial g}{\partial \eta_x}(s_1 |\nabla \theta| + \frac{s_2}{2} |\nabla \theta|^2) \right] \\ \frac{\partial \eta_v}{\partial t} &= \nabla \cdot M_{\eta_v} \nabla \left[ \frac{\partial f}{\partial \eta_v} - a_v^2 \nabla^2 \eta_v - \frac{a_d^2}{2} \nabla^2 \eta_x \right] \\ \frac{\partial [V_i^z]}{\partial t} &= \nabla \cdot M_{[V_i^z]} \nabla \left[ \frac{\partial f}{\partial [V_i^z]} + Z_i e \phi \right] \end{aligned} \quad (2)$$

Here, the sintering phase is able to undergo an  $\eta_x \rightarrow \eta_d$  transition,

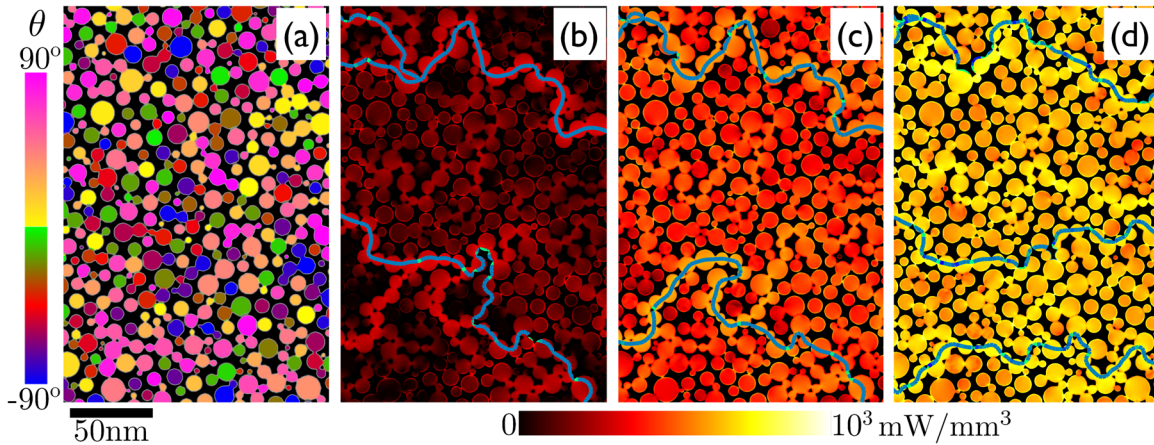


**Fig. 2 Joule heating distribution of a ceramic green body during flash sintering.** Inset (a) shows a section of the 3YSZ microstructure as shown in region (II) in Supplementary Fig. 1. Inset (b) illustrates the spatial distribution of the Joule heating being generated at  $T_f = 1000\text{K}$ . Charge flows through the particle contacts and surfaces (see streamlines). Inset (c) shows the Joule heating at  $T_f = 1200\text{K}$ . As the sample temperature increases, charge flow is suppressed across those particles that develop wider depletion zones, while locally finding surficial and small angle grain boundaries that favor charge transport. Inset (d) shows that at  $T_f = 1300\text{K}$ ,  $[V'_0]$  greatly increases at the grain boundary cores, which promotes charge to flow in a larger number of percolating paths. The increase in charge transport paths further increase the local Joule heating and results in the onset of flash.

and defines a non-conserved order-disorder phase transformation<sup>48,50</sup>. Similarly, the crystallographic orientation of every granular particle is a non-conserved quantity<sup>48,50</sup>. In contrast, the porous phase,  $\eta_v$ , and the concentration of solute and point defects in the condensed phase are conserved quantities<sup>43,44,49</sup>. The structural discontinuity at the pore-condensed phase interface favors the accumulation of charged defects and enables the possibility of a charged surface. The concentration of solute and point defects in the condensed phase are conserved, in agreement with several authors<sup>43,44,49</sup>. In the absence of free surfaces or porosity, and in the limit of a single component system, Eq. (2) reduces to the work by Kobayashi et al.<sup>48</sup>.

For an externally applied electric field, the spatial inhomogeneity in conductivity of the green body due to particle-particle contacts and pore surfaces<sup>47</sup> induces local voltage gradients, which constitute electrostatic deviations,  $\delta\phi$ , away from the equilibrium potential. The total local electrical potential,  $\phi_T$ , is defined as  $\phi_T = \phi + \delta\phi$ , is a solution of Coulomb's Equation (Eq. (7) in the "Methods" section). Here, the homogeneous solution,  $\delta\phi$  is a deviation away from the equilibrium electrostatic potential,  $\phi$ . The solution to the homogeneous part of Coulomb's Equation is calculated using the charge continuity equation:

$$\frac{\partial\rho}{\partial t} = \nabla \cdot \kappa \nabla(\delta\phi), \quad (3)$$

where  $\kappa = \sum_{i=1}^N \frac{e^2 Z_i^2 [V_i^{Z_i}] D_i}{k_b T}$ , is the total electrical conductivity, and  $D_i = D_i^\circ [V_i^{Z_i}] \exp(-\frac{E_{a,i}([V_i^{Z_i}](X))}{k_b T})$ .

The temperature evolution of a green body due to oven-imposed heating is described by the homogenized heat transport equation<sup>51</sup>:

$$\frac{\partial\langle T \rangle}{\partial t} = \langle \kappa \rangle (\nabla \langle \delta\phi \rangle)^2 + \sigma_e e A (T_f^4 - \langle T \rangle^4) + \Delta H^{\times \rightarrow d} \frac{\partial\langle \eta_x \rangle}{\partial t}, \quad (4)$$

where the right-hand side of Eq. (4) embodies the contributions from Joule heating, as the statistical ensemble of microstructural features generated by the ceramic green body during the period leading to the flash event, defined herein as the flash incubation period. Here,  $\langle \kappa \rangle$  is average electrical conductivity,  $\nabla \langle \delta\phi \rangle$  is externally applied macroscopic voltage drop across a width of the sample,  $\sigma_e e A (T_f^4 - \langle T \rangle^4)$  for radiation losses, and  $\frac{\partial\langle \eta_x \rangle}{\partial t}$  accounts for the coarse grained rate of change of order-disorder phase transitions. In the absence of bulk defects and order-disorder

phase transitions, Eq. (4) reduces to existing thermal runaway models for flash sintering, e.g., refs 23–25. See Supplementary Numerical Implementation section for numerical details and Supplementary Table 1 for material properties.

## RESULTS

Figure 2 summarizes the effect of Eqs. (1) through (4) on particle contacts, free surfaces, and triple junctions of a statistically representative green body on the charge transport and Joule heating subjected to a constant heating rate of 10 K/min and an applied electric field of 60 V/cm. Here, when the furnace reaches a temperature of  $T_f = 1000\text{K}$  (see Fig. 2a), the local particle wetting is accompanied by interfacial structural disorder, which in turn induces the formation of a spatial distribution of contact areas that enable charge to percolate across a random distribution of particles. In agreement with previous work<sup>46</sup>, the increase in temperature at the particle-particle contacts provides vibrational energy to the oxygen vacancies, kinetically enabling these defects to segregate to surfaces and interfaces, as a result of the driving force imposed by the high interfacial energy value. The resultant electrochemical state induces an interfacial attraction of  $[Y'_{\text{Zr}}]$  due to its opposite charge polarity. This results in the development of a positive electrostatic interfacial potential as the sample is heated up towards the flash event. Calculations demonstrate that only those particle contacts and surfaces that spatially percolate with locally higher ionic conductivity will control the transport of ions. Figure 2b shows that for a set of stream lines seeded at representative starting points on the far left edge of the sample, the resultant charge transport paths favor contact areas with locally higher ionic conductivity. Further, note that in very tortuously connected regions the most efficient path for charge flux corresponds to surfaces and triple junctions.

As the furnace temperature increases, e.g., to  $T_f = 1200\text{K}$ , the concentration of oxygen vacancies at the large-angle particle contact interfaces increase resulting in the spontaneous appearance of fast ionic conducting paths, which compete for efficient charge flow with the already established particle contacts. As a result, when a local ion transport path becomes shorter than an already established route, charge flux is locally rerouted, micro-structurally improving the Joule heating process (see Fig. 2c).

When the furnace increases its temperature to  $T_f = 1300\text{K}$ , the number of ionic conducting paths that favorably contribute to the

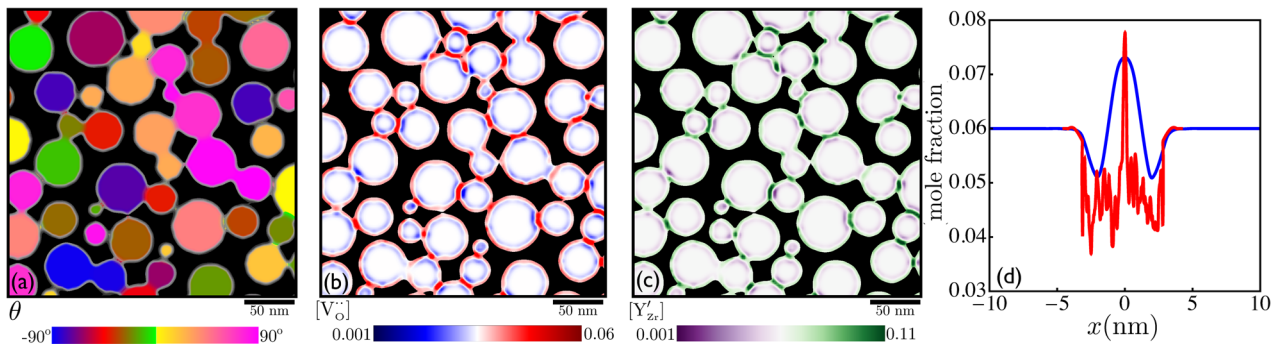


**Fig. 3 Defect distribution of a ceramic green body during flash sintering.** Inset (a) shows the microstructure of 3YSZ sample at a furnace temperature,  $T_f = 1200\text{K}$  (gray box (III) of Supplementary Fig. 1). Inset (b) shows  $[V_O]$  distribution, (c) shows  $[Y_{\text{Zr}}]$  distribution. Inset (d) directly compares the EDS measurement (red) and phase field prediction (blue) of the  $[Y_{\text{Zr}}]$  spatial distribution in the vicinity of a particle-particle contact, for a tilt misorientation,  $\Delta\theta = 30^\circ$ . The segregation of  $[Y_{\text{Zr}}]$  at the triple junctions, particle contacts, and surfaces are in good agreement with EDS results in Fig. 1e–g. The particle-particle contacts and free surfaces accumulate  $[V_O]$  due to thermally enabled chemical driving forces, which naturally attracts the  $[Y_{\text{Zr}}]$  due to its opposite charge polarity.

Joule heating generation increases. Large sections of favorable transport path are dominated by charge flow along particle surfaces. The increase in the number of particle network paths as the temperature increases enables the granular microstructure to transition from being externally heated by the furnace to increasing its internal temperature through self-generated Joule heating. Here, particle-particle contacts and triple junctions generate a lot of Joule heating as a result of the high self-induced electrical conductivity in the interfaces and surfaces, in 3YSZ, defining a random distribution of hot spots. Further, the localized Joule heating favors particle-particle wetting for low angle misorientation locations, while decreasing it for those particle contacts with high angle misorientations. Thus, heating of the sample induced by the imposed electrical current favors necking formation and particle contacts, much before the flash event takes place, in agreement with experiments<sup>18</sup>. Finally, the rapid heating of a green body induced by the current density can initiate a faster densification process, as experimentally observed<sup>26,27</sup>. Overall, the performed analysis demonstrates that the incubation of the flash event is a result of the accumulation of point defects at particle contacts and surfaces in the 3YSZ system, effectively controlling the flash event by heating up the sample through the internal percolating charge conducting paths, which in turn increases the density of efficient Joule heating generating centers.

The compounding effects from the different surfaces and particle-particle contacts, including particle size polydispersity, long-range particle interactions, curvature effects, and the effects of the applied macroscopic voltage, define microstructural deviations from ideality and add inhomogeneities to the spatial distribution of  $[Y_{\text{Zr}}]$ , and  $[V_O]$ , and the corresponding charge flux, during the flash event. Figure 3 shows the spatial distribution of yttrium and oxygen vacancies for a region in a randomly distributed particle population possessing a lognormal size distribution, as one would expect in a commercial powder<sup>52</sup>, for a furnace temperature  $T_f = 1200\text{K}$ . The internal particle contacts display charge accumulation and depletion regions, as described herein; however, contact areas and interfacial curvature develop as a result of the misorientation-controlled wetting of the particles. These developing interfaces induce local microstructural  $[Y_{\text{Zr}}]$  and  $[V_O]$  inhomogeneities that directly impact the position-dependent ionic conductivity. Simulations demonstrate that small contact areas develop a higher concentration of yttrium and oxygen vacancies; however, corner effects (junctions) dominate the segregation of the interface and shift the  $[Y_{\text{Zr}}]$  to a preferential corner. In addition, the vicinity of contact areas with negative radius of curvature become more depleted. Finally, particles

whose diameter is comparable to the width of the electrochemically active area become fully depleted of yttrium and oxygen vacancies, making their core ionically very insulating.

Figure 3d directly compares the predicted and experimental  $[Y_{\text{Zr}}]$  spatial distribution in the vicinity of a particle-particle contact, for a tilt misorientation,  $\Delta\theta = 30^\circ$ , demonstrating a very good agreement. The predicted extent of depletion zone is  $\sim 3.3\text{ nm}$ , in good agreement with experimental value,  $\sim 3.1\text{ nm}$ . Observed differences are a result of the limitations to measure grain boundary core thickness, as spatially resolved by EDS. Further, free surfaces also display a nonuniform distribution of charge. The vicinity of surfaces close to triple junctions display a larger amount of  $[Y_{\text{Zr}}]$  and  $[V_O]$ , as point charges tend to segregate to edges and corners. These surficial heterogeneities are also a function of curvature differences between the particles in contact. Thus, surfaces with smaller radius of curvature will prefer to segregate less charge. The triple junctions are structurally more disordered than surfaces and particle contacts and accumulate larger amounts of  $[V_O]$  and  $[Y_{\text{Zr}}]$  in agreement with EDS results in Fig. 1e, f, and g. A direct comparison against the existing isolated internal pores demonstrates that  $[Y_{\text{Zr}}]$  segregates at surfaces and interfaces, and that  $[V_O]$  correlates directly with its accumulation and depletion.

Figure 4a shows the predicted macroscopic sample temperature,  $T_s$ , and sintering time as a function of furnace temperature,  $T_f$ , for an externally applied electric field of  $60\text{ V/cm}$ . The sample temperature linearly increases during the first  $3000\text{ s}$  as a result of the oven-induced radiation heating. Here, the initial particle contacts and surfaces of percolated particles are formed, as demonstrated herein. The charge flow that is established through the percolating paths contributes to increase the Joule heating and electric power density of the sample. At  $T_f = T_s = 1120\text{K}$ , a kinetic microstructural transition is induced and enables the internal heating of the sample to be self sustained (see Fig. 4b), radiating heat back to the furnace. In this regime, the sample temperature becomes increasingly higher than the furnace temperature. The sample undergoes a thermal and electrical runaway at  $T_{\text{on}} = 1312\text{K}$ , which is defined herein as the onset of flash sintering. While the sample internally heats up at temperatures that are higher than the oven temperature, surfaces and interfaces become increasingly disordered, but interfacial melting is never favored energetically.

The corresponding average predicted current density,  $\langle I \rangle$ , as a function of furnace temperature is shown in Fig. 4c, and highlights that the total conductivity of the heated sample follows an Arrhenius-type response as a function of sample temperature, with an activation energy corresponding to the majority charge

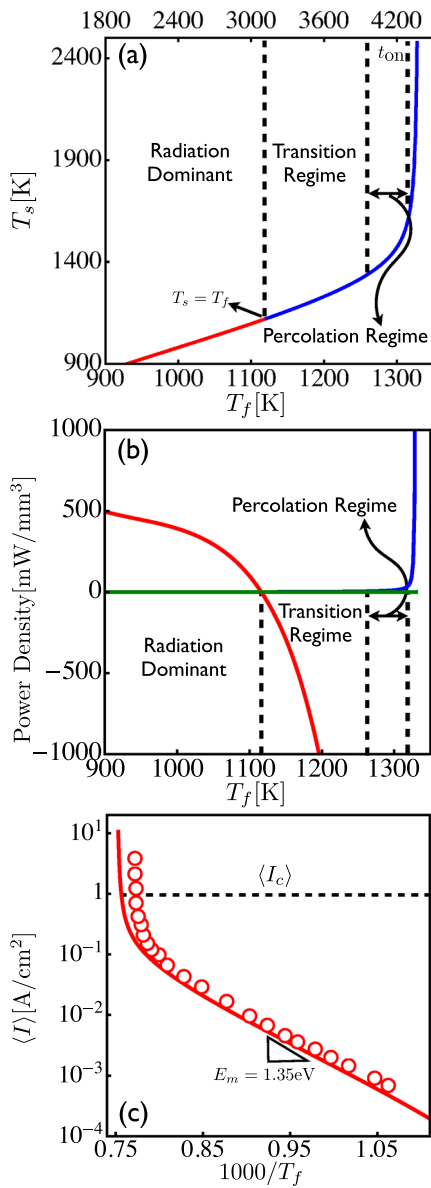


**Fig. 4 Macroscopic Joule heating response of a ceramic green body during flash sintering.** Macroscopic thermal and electrical behavior of 3YSZ sample as described by microstructurally averaging the Joule heating power density response of the simulated ceramic green body (see Fig. 2). Inset (a) shows the predicted sample temperature,  $T_s$ , as a function of furnace temperature,  $T_f$ , and sintering time. An external electric field of 60 V/cm and a constant heating rate of furnace, 10 K/min is applied. Inset (b) shows the different heating rate contributions to heating the sample: radiation heating (red), Joule heating (blue), and enthalpy of melting (green). Inset (c) shows predicted current density,  $\langle I \rangle$ , as a function of furnace temperature. The current density follows an Arrhenius relationship with the sample temperature till incubation time. The abrupt increase in conductivity after the incubation time defines a thermal and electrical runaway, which in turn defines the onset of the flash event.

carrier, the oxygen vacancies energy of migration,  $E_m = 1.35\text{ eV}$ . The predicted critical current density is  $\sim 1.0\text{ A/cm}^2$  in excellent agreement with experimental results<sup>18</sup>.

The compounding effects demonstrated in Figs. 2–4 result in the predicted macroscopic power density response, as shown in Fig. 1a as a function of furnace temperature and time for 3YSZ for a constant heating rate of 10 K/min and an applied electric field of

60 V/cm. A direct comparison to experimental results as reported by Cologna et al.<sup>5</sup> shows an excellent agreement. For these conditions, and as a result of the underlying microstructural fields, the flash temperature is identified herein as  $T_s \sim 1312\text{K}$ , a few degrees away,  $\sim 1300\text{K}$ , as compared to existing coarse-grain thermal runaway models<sup>23–25</sup>. The predicted incubation time for the flash event is  $\sim 4230\text{s}$ . The increase in applied electric field to 120 V/cm reduces the onset flash temperature to  $\sim 1125\text{K}$  and incubation time to  $\sim 3040\text{s}$ . The average current density shows that the total conductivity follows an Arrhenius-type behavior as a function of the sample temperature, as the sample builds up to the flash event. At the microstructural level, HAADF-STEM (see Fig. 1b-d) and EDS mapping (see Fig. 1e-g) of flash sintered 3YSZ samples subjected to an applied electric field of 60 V/cm, demonstrates the  $[Y_{\text{Zr}}]$  segregation at pore surfaces, interfaces, and triple junctions (see Supplementary Experimental Setup for more details). The  $[Y_{\text{Zr}}]$  segregation in polycrystalline 3YSZ is a result of positively charged interfaces due to excess  $[V_O]$ . Also,  $[Y_{\text{Zr}}]$  segregation alters the  $[V_O]$  distribution at interfaces and enhances the ionic conductivity along the interfaces could potentially lead to a flash event<sup>47</sup>. Therefore, Fig. 1a highlights that the critical power density necessary to reach the flash event corresponds to a microstructural self-induced state favored by the Joule heating advent of percolative ionically conductive particle networks. Thus, as the electric field increases, the power density necessary to incubate this state decreases hyperbolically.

## DISCUSSION

A thermodynamically consistent phase-field theory was demonstrated to rationalize the underlying microstructural mechanisms leading to the flash event in great agreement with experimental results. The structural, chemical, and electrostatic interactions of point defects are directly correlated with the intrinsic surfaces and interfaces which control the incubation kinetics of electric field-assisted sintering. Three regimes leading to the onset of flash were identified: (1) Radiation dominated regime, where the initial contacts and surfaces of particles are established and enable charge to start to flow as a result of the heat gained from the oven thermal radiation; (2) Transition regime, where wide depletion zones of  $[V_O]$  and  $[Y_{\text{Zr}}]$  form in the neighborhood of large-angle contacts between particles, impeding the charge flow across particles where charge was previously favored, deflecting it to new surficial and small-angle interfaces. Here, the contribution to the Joule heating of the sample continuously increases and dominates to increase the temperature of the sample over external radiation heating. Finally, (3) Percolating regime, where  $[V_O]$  increases drastically at the core of the particle contacts, surfaces, and triple junctions allows charge along flow in multiple percolative paths, transitioning from interfacially-driven Joule heating to volumetric-driven Joule heating, resulting in a flash event.

The developed theory mainly focuses on explaining the incubation kinetics alone, i.e., only the build-up process to the flash event. Important effects occurring after the incubation event has resulted in a flash event, such as time-dependent elastic and plastic flow kinetics, densification, and grain growth during and after the flash event are beyond the scope of this work. The current variational formulation sets the stage to understand the densification and grain growth kinetics during the flash event by introducing the rates of generation, reaction, and sink of oxygen vacancies and cation vacancies, which can be readily incorporated in densification models, as reported by several authors, e.g., refs 53–55. Also, rigid body motion of powder particles are not considered but can be introduced in the existing model to describe the mass transport during densification and grain coarsening kinetics, as reported by several authors, e.g., refs 55,56.

The current formulation is demonstrated on 3YSZ and can be readily extended to other chemistries, such as 8YSZ and ZnO by incorporating the correct thermodynamic and kinetic data. Recent work, e.g., ref. <sup>47</sup>, and well established first principles studies<sup>57</sup>, demonstrate that the grain boundary ionic transport properties for 3YSZ can be enhanced, while the attractive interactions between  $[V_O]$  and  $[Y_{Zr}]$  drop the ionic mobility of oxygen vacancies in 8YSZ, and lead to a significant decrease in the local particle-particle interfacial ionic conductivity. Finally, the application of the theoretical approach proposed herein to other chemistries will enable a detailed understanding on the generality, limits, and applications of flash sintering of single crystals and powder specimens<sup>28</sup>, including different particle sizes, morphologies and textures of powder specimens.

Overall, the developed theory provides a fundamental basis to engineer the microstructural evolution and charge transport of ionic ceramic green bodies before and during electric-field assisted sintering for a wide variety of technologically advanced ceramics, such as solid oxide fuel cells, solid state-based lithium-ion batteries, and high-temperature gas sensors.

## METHODS

### Theoretical framework

Define the Helmholtz free energy density,  $f$ , of an ionic ceramic green body for three distinct microstructural regions: the solid crystalline lattice,  $\eta_x$ , the structurally disordered, interfacial disordered regions,  $\eta_d$ , and those regions describing the open and closed porosity,  $\eta_v$ . Site conservation is imposed on the system through the expression,  $\eta_x + \eta_d + \eta_v = 1$ .  $f$  is a function of  $N$  chemical species,  $\{[V_1^Z], \dots, [V_N^Z]\}$ <sup>50</sup>. The thermochemical volumetric free energy based on equilibrium defect principles<sup>58,59</sup> is defined herein as

$$\begin{aligned} f(\eta_x, \eta_d, \eta_v, [V_1^Z], \dots, [V_N^Z], T) = & \frac{1}{\nu} \left( \sum_{i=1}^N (f_i(\eta_x, \eta_d, \eta_v, T)[V_i^Z] + k_b T [V_i^Z] \ln [V_i^Z]) \right. \\ & + k_b T (1 - \sum_{i=1}^N [V_i^Z]) \ln [1 - \sum_{i=1}^N [V_i^Z]] + \sum_{j=1, j \neq i}^N \Omega_j [V_i^Z] [V_j^Z]) \\ & \left. + \sum_{i,j}^N w_{ij} h(\eta_i, \eta_j) + \Delta H^{x \rightarrow d} \frac{\partial T}{\partial m} p(\eta_x) \right) \end{aligned} \quad (5)$$

The free energy of formation of the  $i$ th species is  $f_i(\eta_x, \eta_d, \eta_v, T) = f_i^x(T)p(\eta_x) + f_i^d(T)p(\eta_d) + f_i^v(T)p(\eta_v)$ , where  $f_i^x$  corresponds to the formation energy of  $i$ th species in the crystalline lattice,  $f_i^d$  to the disorder phase, and  $f_i^v$  to the pore phase.  $p(\eta_i) = \frac{1}{2} \eta_i^2 (15 - 25\eta_i + 15\eta_i^2 - 3\eta_i^3 - 15(1 - \eta_i) \sum_{j \neq i} \eta_j^2)$  is an interpolation function<sup>60</sup>,  $h(\eta_i, \eta_j) = \eta_i^2 \eta_j^2$  is a pair wise function to prevent spontaneous phase transformations, and  $w_{ij}$  is the energy barrier height. In the present study, two major species are considered, i.e., oxygen vacancies,  $[V_O]$ , and yttrium defects,  $[Y_{Zr}]$ . The concentration of cation vacancies and cation interstitials are between two to nine orders of magnitude smaller than that of  $[V_O]$  and  $[Y_{Zr}]$ , based on the existing experimental and DFT studies<sup>61–63</sup>. Other impurities, precipitates, and defects can be incorporated into this model through well established thermodynamic principles, i.e., by editing Eq. (5), and through the introduction of phase-field descriptions that capture the formation of new phases<sup>57,64–66</sup>. In the absence of electrical effects for a binary system, Eq. (5) reduces to neutral grain boundary complexions formulation by Tang et al.<sup>58</sup>. In the absence of electrostatic interactions in a single component system, Eq. (5) reduces to the multiphase field model, as pioneered by Steinbach et al.<sup>67</sup>.

In agreement with recent work<sup>44,46,47</sup>, the extended free energy density,  $f_e$ , is a function of the electrostatic potential,  $\phi$ , the electrostatic charge per unit volume,  $\rho$ , the electric displacement field vector,  $\vec{D}$ , and the electric field vector,  $\vec{E}$ , which allows to formulate contributions from the electrostatic charge energy density,  $\rho\phi$ , and the dipolar energy density,  $\frac{1}{2} \vec{D} \cdot \vec{E}$ :  $f_e(\eta_x, \eta_d, \eta_v, [V_1^Z], \dots, [V_N^Z], \rho, \vec{D}, T) = f(\eta_x, \eta_d, \eta_v, [V_1^Z], \dots, [V_N^Z], T) + \rho\phi + \frac{1}{2} \vec{D} \cdot \vec{E}$ .

By performing the Legendre transform,

$$f_{ec}(\eta_x, \eta_d, \eta_v, [V_1^Z], \dots, [V_N^Z], \vec{E}, T) = f_o(\eta_x, \eta_d, \eta_v, [V_1^Z], \dots, [V_N^Z], \vec{D}, T) - \vec{D} \cdot \vec{E} \quad (6)$$

on  $f_e$ , the electrochemical free energy density,  $f_{ec}$ , is minimized<sup>59,68</sup>. Physical constraints, such as  $\vec{E} = -\nabla\phi$  (a solution to Faraday's Law under constant magnetic field), and  $\vec{D} = \epsilon \vec{E} = -\epsilon \nabla\phi$  (a constitutive law for

electrically active systems in the absence of pyroelectricity and ferroelectricity), are directly substituted in Eq. (6).

The crystallographic orientation in each single-crystal particle in the ionic ceramic green body is described using the order parameter,  $\theta$ . The interfacial energy from particle contacts due to local misorientation,  $|\nabla\theta|$ , is incorporated by extending the KWC model<sup>48</sup>. Two terms contributing to particle contacts interfacial energy are:  $s_1 g(\eta_x) |\nabla\theta|$ , and  $\frac{s_2}{2} g(\eta_x) |\nabla\theta|^2$ . Here,  $g(\eta_x) = \eta_x^2$  is a coupling function, and  $s_1$  and  $s_2$  are structural parameters, as proposed by Warren et al.<sup>69</sup>. The sum of the contributions from thermochemical, electrical, and interfacial energy to the total free energy functional is given by Eq. (1).

In agreement with recent work<sup>46,47</sup>, Eq. (1) defines the equilibrium of a polycrystalline ceramic with electrostatically active grain boundaries and free surfaces by minimizing the free energy functional with respect to the controlling variables,  $\{[V_j^Z]\} = \{[V_1^Z], \dots, [V_N^Z]\}$ ,  $\{\eta_i\} = \{\eta_x, \eta_d, \eta_v\}$ ,  $\theta, \rho, \phi$ . For ease in the description, except for solid  $\leftrightarrow$  liquid phase transitions, and crystallographic order  $\leftrightarrow$  disorder volumetric, conserved or non-conserved, solid-state phase transformations such as chemical phase separation are not included; however, they can be easily incorporated, e.g., see refs<sup>49,58,70,71</sup>. Additional physical constraint on the volumetric charge density to the local composition of the  $i$ th species is  $\rho = \sum_{i=1}^N e Z_i [V_i^Z]$ <sup>43–47</sup>

The variational derivatives of Eq. (1) after substituting  $\eta_d = 1 - \eta_x - \eta_v$  are

$$\begin{aligned} \frac{\delta f}{\delta \theta} &= -g(\eta_x) (s_1 \nabla \cdot \frac{\nabla \theta}{|\nabla \theta|} + s_2 \nabla^2 \theta) \\ \frac{\delta f}{\delta \eta_x} &= \frac{\partial f}{\partial \eta_x} - \alpha_x^2 \nabla^2 \eta_x - \frac{\alpha_d^2}{2} \nabla^2 \eta_v + \frac{\partial g}{\partial \eta_x} (s_1 |\nabla \theta| + \frac{s_2}{2} |\nabla \theta|^2) \\ \frac{\delta f}{\delta \eta_v} &= \frac{\partial f}{\partial \eta_v} - \alpha_v^2 \nabla^2 \eta_v - \frac{\alpha_d^2}{2} \nabla^2 \eta_x \\ \frac{\delta f}{\delta [V_i^Z]} &= \xi_i = \frac{\partial f}{\partial [V_i^Z]} + Z_i \epsilon \phi \\ \frac{\delta f}{\delta \phi} &= \nabla \cdot \epsilon \nabla \phi + \rho = 0 \end{aligned} \quad (7)$$

The first three rows of Eq. (7) define the structural state of every granular volume element of material, including crystalline grains, interfacial particle-particle contact, and internal and external surfaces.  $\xi_i$  in the fourth row of Eq. (7) corresponds to the structural and electrochemical potential<sup>46,47</sup>, and is a local thermodynamic driving force for mass and charge accumulation at the  $i$ th chemical species at particle contacts and surfaces due to local structural, chemical, and electrical inhomogeneities.  $\xi_i$  reduces to electrochemical potential in the absence of local structural inhomogeneities and chemical potential gradients in the absence of electrical effects, in agreement with multiple authors<sup>43–47</sup>. Lastly, the fifth row of Eq. (7) represents Coulomb's equation in its differential form, in agreement with previous work<sup>43–47</sup>.

Locally, for small deviations away from equilibrium, the structural and electrochemical variational derivatives associated to Eq. (1) and Coulomb's Equation constitute the driving forces for microstructural evolution<sup>44,49</sup>. The resultant kinetic equations are summarized in Eq. (2).

The effect of heating imposed by the oven is described by considering the contributions to the enthalpy of the system,  $h = u - \bar{\sigma} \cdot \bar{\epsilon}$ , for a volume element of material, where  $\bar{\sigma}$  is the mechanical stress tensor and  $\bar{\epsilon}$  is the elastic strain tensor. Following Boettger et al.<sup>49</sup>, and in agreement with Eq. (1), the change in enthalpy density is expressed as

$$\begin{aligned} dH(\{\eta_i\}, \{[V_j^Z]\}, \rho, \vec{D}, \sigma, S) = & \sum_{i=1}^M \frac{\partial H}{\partial \eta_i} d\eta_i + \sum_{j=1}^N \mu_j d[V_j^Z] \\ & + \phi dp + \vec{E} \cdot d\vec{D} + TdS - \bar{\epsilon} \cdot d\bar{\sigma} \end{aligned} \quad (8)$$

For an isobaric, or constant stress system, Eq. (8) reduces to  $dH = -\Delta H^{x \rightarrow d} d\eta_x + \sum_{j=1}^N (\mu_j + Z_j \phi) d[V_j^Z] + \vec{E} \cdot d\vec{D} + c_\sigma dT$ . Here,  $dS \sim c_\sigma \frac{dT}{T}$ , where  $c_\sigma$  is the heat capacity per unit volume at constant stress of 1 atm, and  $\Delta H^{x \rightarrow d}$  is the latent heat of melting per unit volume. The generalized change in enthalpy for  $M$  order-disorder phases,  $\sum_{i=1}^M \frac{\partial H}{\partial \eta_i} d\eta_i$ , reduce to  $-\Delta H^{x \rightarrow d} d\eta_x$ , for the case of only one order-disorder phase transition. By applying the enthalpy method<sup>72</sup>, heat balance is readily accounted for as

$$\begin{aligned} \frac{\partial H}{\partial t} &= -\Delta H^{x \rightarrow d} \frac{\partial \eta_x}{\partial t} + \sum_{j=1}^N (\mu_j + Z_j \phi) \frac{\partial [V_j^Z]}{\partial t} + \vec{E} \cdot \frac{\partial \vec{D}}{\partial t} + c_\sigma \frac{\partial T}{\partial t} \\ &= \nabla \cdot (\lambda \nabla T) + \kappa (\nabla \cdot \phi)^2 \end{aligned} \quad (9)$$

Here, Stefan-Boltzmann radiation exchange between the sintered solid and the surrounding oven walls is described by,  $Q_{rad} = \sigma_e A (T_f^4 - T^4)$ , as a boundary condition at the solid-pore interface.  $A$  is the effective surface

area between the sample and the oven walls, and  $\epsilon$  is emissivity of the sintered gray body<sup>73</sup>.

In the limit of a sample whose characteristic physical dimensions are much smaller than the representative thermal diffusion distance,

$$L \ll \sqrt{\frac{\lambda}{c_p} t},$$

and ionic species at steady state,  $\frac{\partial [V_j^z]}{\partial t} \sim 0$ , and in the absence

of electromagnetic waves,  $\frac{\partial \vec{D}}{\partial t} \sim 0$ , Eq. (9) reduces to:

$$\frac{\partial T}{\partial t} = \kappa(\nabla(\delta\phi))^2 + \Delta H^{x-d} \frac{\partial \eta_x}{\partial t} \quad (10)$$

The radiation heat transfer of the internal surfaces of the green body is set to zero since the local thermal gradients across the porous microstructure are effectively zero. Equation (10) results in the homogenized heat transport equation<sup>51</sup>, Eq. (4).

## DATA AVAILABILITY

The simulation data from this study are available upon request.

## CODE AVAILABILITY

The partial differential equations were implemented in FiPy 3.1. The theoretical data from this study is available upon request.

Received: 18 June 2019; Accepted: 4 June 2020;

Published online: 15 July 2020

## REFERENCES

- Rahaman, M. N. *Ceramic Processing and Sintering* (Marcel Dekker, New York, 1996).
- Commission, E. *Reference Document on Best Available Techniques in the Ceramic Manufacturing Industry*. 210–211 (Ceramic Manufacturing Industry, 2007).
- Biesuza, M. & Sglavo, V. M. Flash sintering of ceramics. *J. Eur. Ceram. Soc.* **39**, 115–143 (2019).
- Tuan, W.-H. & Guo, J.-K. *Multiphased Ceramic Materials: Processing and Potential* (Springer, New York, 2004).
- Cologna, M., Rashkova, B. & Raj, R. Flash sintering of nanograin zirconia in <5s at 850 °C. *J. Am. Ceram. Soc.* **93**, 3556–3559 (2010).
- Oghbaei, M. & Mirzaee, O. Microwave versus conventional sintering: A review of fundamentals, advantages and applications. *J. Alloy. Compd.* **494**, 175–189 (2010).
- Downs, J. A. & Sglavo, V. M. Electric field assisted sintering of cubic zirconia at 390 °C. *J. Am. Ceram. Soc.* **96**, 1342–1344 (2013).
- Spiridigliozzi, L. et al. Microstructural and electrical investigation of flash sintered Gd/Sm-doped ceria. *J. Mater. Sci.* **52**, 7479–7488 (2017).
- Hao, X., Liu, Y., Wang, Z., Qiao, J. & Sun, K. A novel sintering method to obtain fully dense gadolinia doped ceria by applying a direct current. *J. Power Sources* **210**, 86–91 (2012).
- Becker, M. Z., Shomrat, N. & Tsur, Y. Recent advances in mechanism research and methods for electric-field-assisted sintering of ceramics. *Adv. Mater.* **30**, 1706369 (2018).
- Wang, H. et al. Key microstructural characteristics in flash sintered 3YSZ critical for enhanced sintering process. *Ceram. Int.* **45**, 1251–1257 (2019).
- Prette, A. L. G., Cologna, M., Sglavo, V. M. & Raj, R. Flash-sintering of Co<sub>2</sub>MnO<sub>4</sub> spinel for solid oxide fuel cell applications. *J. Power Sources* **196**, 2061–2065 (2011).
- Gaur, A. & Sglavo, V. M. Densification of La<sub>0.6</sub>Sr<sub>0.4</sub>Co<sub>0.2</sub>Fe<sub>0.8</sub>O<sub>3</sub> ceramic by flash sintering at temperature less than 100 °C. *J. Mater. Sci.* **49**, 6321–6332 (2014).
- Gaur, A. & Sglavo, V. M. Tuning the flash sintering characteristics of ceria with MnCo<sub>2</sub>O<sub>4</sub>. *Mater. Sci. Eng. B Solid-State Mater. Adv. Technol.* **228**, 160–166 (2018).
- Zapata-Solvias, E., Bonilla, S., Wilshaw, P. R. & Todd, R. I. Preliminary investigation of flash sintering of SiC. *J. Eur. Ceram. Soc.* **33**, 2811–2816 (2013).
- Schmerbauch, C., Gonzalez-Julian, J., Röder, R., Ronning, C. & Guillou, O. Flash sintering of nanocrystalline zinc oxide and its influence on microstructure and defect formation. *J. Am. Ceram. Soc.* **97**, 1728–1735 (2014).
- Zhang, Y. & Luo, J. Promoting the flash sintering of ZnO in reduced atmospheres to achieve nearly full densities at furnace temperatures of <120 °C. *Scr. Mater.* **106**, 26–29 (2015).
- Naik, K. S., Sglavo, V. M. & Raj, R. Field assisted sintering of ceramic constituted by alumina and yttria-stabilized zirconia. *J. Eu. Ceram. Soc.* **76**, 2435–2442 (2014).
- Kok, D., Jha, S. K., Raj, R. & Mecartney, M. L. Flash sintering of a three-phase alumina, spinel, and yttria-stabilized zirconia composite. *J. Am. Ceram. Soc.* **100**, 16–19 (2017).
- Lebrun, J. M. & Raj, R. A first report of photoemission in experiments related to flash sintering. *J. Am. Ceram. Soc.* **97**, 2427–2430 (2014).
- Raj, R. Analysis of the power density at the onset of flash sintering. *J. Am. Ceram. Soc.* **99**, 3226–3232 (2016).
- Yu, M., Grasso, S., McKinnon, R., Saunders, T. & Reece, M. J. Review of flash sintering: materials, mechanisms and modelling. *Adv. Appl. Ceram.* **116**, 24–60 (2017).
- Zhang, Y., Jung, J. I. & Luo, J. Thermal runaway, flash sintering and asymmetrical microstructural development of ZnO and ZnO-Bi<sub>2</sub>O<sub>3</sub> under direct currents. *Acta Mater.* **94**, 87–100 (2015).
- Todd, R. I., Zapata-Solvias, E., Bonilla, R. S., Sneddon, T. & Wilshaw, P. R. Electrical characteristics of flash sintering: thermal runaway of joule heating. *J. Eur. Ceram. Soc.* **35**, 1865–1877 (2015).
- Dong, Y. & Chen, I. Onset criterion for flash sintering. *J. Am. Ceram. Soc.* **98**, 3624–3627 (2015).
- Zhang, Y., Nie, J., Chan, J. M. & Luo, J. Probing the densification mechanisms during flash sintering of ZnO. *Acta Mater.* **125**, 465–475 (2017).
- Ji, W. et al. Ultra-fast firing: effect of heating rate on sintering of 3YSZ, with and without an electric field. *J. Eur. Ceram. Soc.* **37**, 2547–2551 (2017).
- Luo, J. The scientific questions and technological opportunities of flash sintering: from a case study of ZnO to other ceramics. *Scripta* **146**, 260–266 (2018).
- Raj, R. Joule heating during flash-sintering. *J. Eur. Ceram. Soc.* **32**, 2293–2301 (2012).
- Naik, K. S., Sglavo, V. M. & Raj, R. Flash sintering as a nucleation phenomenon and a model thereof. *J. Eur. Ceram. Soc.* **34**, 4063–4067 (2014).
- Jongmanns, M., Raj, R. & Wolf, D. E. Generation of frenkel defects above the debye temperature by proliferation of phonons near the brillouin zone edge. *N. J. Phys.* **20**, 093013 (2018).
- Schie, M., Menzel, S., Robertson, J., Waser, R. & DeSouza, R. A. Field enhanced route to generating anti-frenkel pairs in HfO<sub>2</sub>. *Phys. Rev. Mater.* **2**, 035002 (2018).
- Narayan, J. Grain growth model for electric field-assisted processing and flash sintering of materials. *Scr. Mater.* **68**, 785–788 (2013).
- Narayan, J. A new mechanism for field-assisted processing and flash sintering of materials. *Scr. Mater.* **69**, 107–111 (2013).
- Chaim, R., Chevallier, G., Weibel, A. & Estournés, C. Flash sintering of dielectric nanoparticles as a percolation phenomenon through a softened film. *J. Appl. Phys.* **121**, 145103 (2017).
- Todd, R. I. Flash sintering of ceramics: A short review. *Proc. IV Adv. Ceram. Appl.* (Atlantis Press: Paris, 2017) 1–12.
- M'Peko, J.-C., Francis, J. & Raj, R. Impedance spectroscopy and dielectric properties of flash versus conventionally sintered yttria-doped zirconia electroceramics viewed at the microstructural level. *J. Am. Ceram. Soc.* **96**, 3760–3767 (2013).
- Yoshida, H., Yokoyama, K., Shibata, N., Ikuhara, Y. & Sakura, T. High-temperature grain boundary sliding behavior and grain boundary energy in cubic zirconia bicrystals. *Acta Mater.* **52**, 2349–2357 (2004).
- Shibata, N., Oba, F., Yamamoto, T. & Ikuhara, Y. Structure, energy and solute segregation behavior of [110] symmetric tilt grain boundaries in yttria-stabilized cubic zirconia. *Philos. Mag. Lett.* **84**, 2381–2415 (2004).
- Lee, H. B., Prinz, F. B. & Cai, W. Atomistic simulations of surface segregation of defects in solid oxide electrolytes. *Acta Mater.* **58**, 2197–2206 (2010).
- Lee, H. B., Prinz, F. B. & Cai, W. Atomistic simulations of grain boundary segregation in nanocrystalline yttria-stabilized zirconia and gadolinia-doped ceria solid oxide electrolytes. *Acta Mater.* **61**, 3872–3887 (2013).
- Chen, L. Q. & Khachaturyan, A. G. Dynamics of simultaneous ordering and phase separation and effect of long-range coulomb interactions. *Phys. Rev. Lett.* **70**, 1477–1480 (1993).
- Bishop, C. M., García, R. E. & Carter, W. C. Effect of charge separation on the stability of large wavelength fluctuations during spinodal decomposition. *Acta Mater.* **51**, 1517–1524 (2003).
- García, R. E., Bishop, C. M. & Carter, W. C. Thermodynamically consistent variational principles with applications to electrically and magnetically active systems. *Acta Mater.* **52**, 11–21 (2004).
- Guyer, J. E., Boettinger, W. J., Warren, J. A. & McFadden, G. B. Phase field modeling of electrochemistry I: equilibrium. *Phys. Rev. E.* **69**, 021603 (2004).
- Vikrant, K. S. N., Chueh, W. C. & García, R. E. Charged interfaces: electrochemical and mechanical effects. *Energy Environ. Sci.* **11**, 1993–2000 (2018).
- Vikrant, K. S. N. & García, R. E. Charged grain boundary transitions in ionic ceramics for energy applications. *npj Comput. Mater.* **5**, 1–12 (2019).
- Kobayashi, R., Warren, J. A. & Carter, W. C. A continuum model of grain boundaries. *Phys. D.* **140**, 141–150 (2000).
- Boettinger, W. J., Warren, J. A., Beckermann, C. & Karma, A. Phase-field simulation of solidification. *Annu. Rev. Mater. Res.* **32**, 163–194 (2002).
- Tang, M., Carter, W. C. & Cannon, R. M. Diffuse interface model for structural transitions of grain boundaries. *Phys. Rev. B: Condens. Matter Mater. Phys.* **73**, 024102 (2006).

51. Auriault, J. L. & Royer, P. Double conductivity media: a comparison between phenomenological and homogenization approaches. *Int. J. Heat. Mass Transf.* **36**, 2613–2621 (1993).
52. Vaz, M. F. & Fortes, M. A. Grain size distribution: The lognormal and the gamma distribution functions. *Scr. Metall.* **22**, 35–40 (1988).
53. Rehn, V. et al. Phase-field study of grain growth in porous polycrystals. *Acta Mater.* **174**, 439–449 (2019).
54. Li, Y., Hu, S., Sun, X. & Stan, M. A review: applications of the phase field method in predicting microstructure and property evolution of irradiated nuclear materials. *npj Computational Mater.* **3**, 16 (2017).
55. Dzepina, B., Balint, D. & Dini, D. A phase field model of pressure-assisted sintering. *J. Eur. Ceram. Soc.* **39**, 173–182 (2019).
56. Wang, Y. U. Computer modeling and simulation of solid-state sintering: A phase field approach. *Acta Materialia* **54**, 953–961 (2006).
57. Pornprasertsuk, R., Ramanarayanan, P., Musgrave, C. B. & Prinz, F. B. Predicting ionic conductivity of solid oxide fuel cell electrolyte from first principles. *J. Appl. Phys.* **98**, 103513 (2005).
58. Tang, M., Carter, W. C. & Cannon, R. M. Grain boundary transitions in binary alloys. *Phys. Rev. Lett.* **97**, 075502 (2006).
59. DeHoff, R. T. *Thermodynamics in Materials Science*. 2nd (McGraw-Hill, New York, 1993).
60. Pogorelov, E., Kundin, J. & Emmerich, H. General phase-field model with stability requirements on interfaces in N-dimensional phase-field space. arXiv preprint arXiv:1304.6549, 1–13 (2013).
61. Kilo, M., Jackson, R. A. & Borchardt, G. Computer modelling of ion migration in zirconia. *Philos. Mag.* **83**, 3309–3325 (2003).
62. Kilo, M. et al. Modeling of cation diffusion in oxygen ion conductors using molecular dynamics. *Solid State Ion.* **175**, 823–827 (2004).
63. Dong, Y., Qi, L., Li, J. & Chen, I.-W. A computational study of yttria-stabilized zirconia: II. Cation diffusion. *Acta Materialia* **126**, 438–450 (2017).
64. Romero, R. L. G., Melendez, J. J., García, D. G., Cumbra, F. L. & Rodriguez, A. D. Segregation to the grain boundaries in YSZ bicrystals: a molecular dynamics study. *Solid State Ion.* **237**, 8–15 (2013).
65. Zhu, J. Z., Liu, Z. K., Vaithyanathan, V. & Chen, L. Q. Linking phase-field model to CALPHAD: an application to precipitate shape evolution in Ni-base alloys. *Scr. Materialia* **46**, 401–406 (2002).
66. Ozturk, K. et al. Linking first-principles energetics to CALPHAD: an application to thermodynamic modeling of the Al-Ca binary system. *Metall. Mater. Trans. A* **36A**, 5–13 (2005).
67. Steinbach, I. et al. A phase field concept for multiphase systems. *Phys. D.* **94**, 135–147 (1996).
68. Gibbs, J. W. On the equilibrium of heterogeneous substances. *Phys. Rev.* **44**, 108–437 (1878).
69. Warren, J. A., Kobayashi, R., Lobkovsky, A. E. & Carter, W. C. Extending phase field models of solidification to polycrystalline materials. *Acta Mater.* **51**, 6035–6058 (2003).
70. Cahn, J. W. & Hilliard, J. E. Free energy of a nonuniform system. I. Interfacial free energy. *J. Chem. Phys.* **28**, 258–267 (1958).
71. Cahn, J. W. On spinodal decomposition. *Acta Metall.* **9**, 795–801 (1961).
72. Shamsundar, N. & Sparrow, E. M. Effect of density change on multidimensional conduction phase change. *ASME J. Heat. Transf.* **98**, 550–557 (1976).
73. Incropera, F. P., DeWitt, D. P., Bergman, T. L. & Lavine, A. S. *Fundamentals of Heat and Mass Transfer* (John Wiley & Sons, 2007).

## ACKNOWLEDGEMENTS

The authors are very grateful for the support provided by US ONR N00014-17-1-2087.

## AUTHOR CONTRIBUTIONS

K.S.N.V. and R.E.G. jointly developed the theoretical formulation. H.W. and H.W. carried out the electric field-assisted sintering experiments. A.J. provided the green body microstructure for the numerical simulations. K.S.N.V. wrote and performed the numerical simulations shown herein. K.S.N.V. also compared the calculated results against experimental data under the guidance of REG.

## COMPETING INTERESTS

The authors declare no competing interests.

## ADDITIONAL INFORMATION

**Supplementary information** is available for this paper at <https://doi.org/10.1038/s41524-020-00359-7>.

**Correspondence** and requests for materials should be addressed to R.E.G.

**Reprints and permission information** is available at <http://www.nature.com/reprints>

**Publisher's note** Springer Nature remains neutral with regard to jurisdictional claims in published maps and institutional affiliations.



**Open Access** This article is licensed under a Creative Commons Attribution 4.0 International License, which permits use, sharing, adaptation, distribution and reproduction in any medium or format, as long as you give appropriate credit to the original author(s) and the source, provide a link to the Creative Commons license, and indicate if changes were made. The images or other third party material in this article are included in the article's Creative Commons license, unless indicated otherwise in a credit line to the material. If material is not included in the article's Creative Commons license and your intended use is not permitted by statutory regulation or exceeds the permitted use, you will need to obtain permission directly from the copyright holder. To view a copy of this license, visit <http://creativecommons.org/licenses/by/4.0/>.

© The Author(s) 2020